

Thermo-elasto-hydrodynamic analysis of bump-type air foil thrust bearings considering misalignment

Markus Eickhoff[✉], Johannis Triebwasser, and Bernhard Schweizer*

Institute of Applied Dynamics, Technical University of Darmstadt, Germany

Abstract. In this study, a multi-pad bump-type foil thrust bearing with a taper-land height profile is investigated. A detailed thermo-elasto-hydrodynamic (TEHD) finite element (FE) model is used comprising all bearing pads instead of only a single pad. Although the single-pad reduction approach is commonly applied, it can not accurately account for the different temperatures, loads, and power losses for individual pads in the case of misalignment. The model accounts for the deformations of the foils on each pad via a Reissner-Mindlin-type shell model. Deformations of the rotor are calculated via the Navier-Lamé equations with thermoelastic stresses and centrifugal effects. The temperature of the top foil and the rotor are calculated with the use of heat diffusion equations. The temperature of each lubricating air film is obtained through a 3D energy equation. Film pressures are calculated with the 2D compressible Reynolds equation. Moreover, the surrounding of the bearing and runner disk is part of the thermodynamic model. Results indicate that the thermal bending of the runner disk as well as top foil sagging are key factors in performance reduction. Due to the bump-type understructure, the top foil sagging effect is observed in simulation results. The study at hand showcases the influence of misalignment between the rotor and the bearing on the bearing performance.

Key words: air foil thrust bearing; simulation; misalignment.

1. INTRODUCTION

Foil bearing technology has its roots over half a century ago, when foil bearings were developed for the use in air cycle machines in aviation, [1,2]. With an increasing demand in sustainable and oil-free technology today, the use of air foil bearings gains popularity quickly. Further advantages of these bearings consist in their reliability and their tolerance of manufacturing errors as well as misalignment of the rotor system.

In a machine application, the air foil thrust bearing (AFTB) is usually integrated in the stationary machine housing. The rotor possesses a smooth rotor disk acting as a counterpart. As the rotor disk starts to rotate, an air stream into the wedge-shaped lubricating gap between the rotor disk and the bearing surface is created. The generated pressure can eventually carry the thrust loads acting upon the rotor system. For lower speeds, dry friction occurs so that top foil and rotor coatings are used [3,4]. In comparison to rigid air bearings, foil air bearings possess lower load capacities due to nonuniform bump foil deformations and foil sagging effects.

The investigation of AFTB performance has been conducted by numerous authors in the past. Experimental testing plays a key role in the analysis, see e.g. [5–7].

With numerical models, the foil thrust bearing behavior can be studied and optimized in great detail, see e.g. [8–15].

The thrust foil bearing design with multiple pads and a nominal taper-land topology has been the focus of previous works,

cf. [16–18]. In this study, the influence of misalignment on the bearing performance is studied in a detailed TEHD FE model, which requires the following substantial extensions:

- When considering misalignment, the height function of each bearing pad is individual.
- Each bearing pad exerts a different pressure load and power loss.
- Therefore, the analysis of a single bearing pad as a representation for the overall bearing behavior is no longer valid. The successive calculation of each bearing pad individually is sufficient only for the isothermal case. For the thermal model of the bearing, the fully coupled model of all individual air films presented in this paper can solve this issue.
- Through the use of a single rotor model combined with multiple individual bearing pads (air films and foil understructure), the case of misalignment is adequately represented in the thrust bearing model.
- This extension displays huge additional computational expenses. In comparison with a reduced model where only a single bearing pad is taken into account, computation times are increased by a factor of 8–10 when considering a bearing with six bearing pads.

In this manuscript, a description of the thrust bearing model is given in Section 2. Section 3 presents numerical results for simulations considering misalignment of the rotor disk. The paper is concluded in Section 4.

2. THRUST BEARING MODEL

This section presents the fully coupled TEHD model for the analysis of the AFTB. The bearing design of the current study is displayed in Fig. 1. The rotor possesses a smooth rotor disk

*e-mail: eickhoff@ad.tu-darmstadt.de

Manuscript submitted 2023-05-05, revised 2023-08-22, initially accepted for publication 2023-10-02, published in December 2023.

which is mounted opposite to the thrust bearing of Fig. 1a. The bearing consists of a base plate and 6 individual bearing pads with one bump foil and one top foil each. The bump foil is made up of 3 bump strips with three, four, and five bumps, respectively. The bumps of the bump foil are arranged parallel to the trailing edge of the top foil. The bump foil creates a compliant understructure for the smooth top foil. Through the use of bumps with specific heights, a taper-land height profile is created as depicted in Fig. 1b. The land area is flat, while the taper region ascends from the fixation at the leading edge towards the transition line. The angular velocity Ω of the rotor is marked in Fig. 1b. Figure 2 shows the assembly of the rotor in a cut view with the different model components. Note that the bearing in this analysis possesses an outer diameter of 60 mm.

The model contains the calculation of the air film pressure in the lubricating air gap between the rotor disk and the top foils (Section 2.1), the calculation of bump and top foil deformations (Section 2.2) as well as rotor disk deformations (Section 2.3), the calculation of the air film temperature (Section 2.4), and the calculation of the rotor temperature (Section 2.5) as well as the

top foil temperature (Section 2.6). The section is finished by details on the air film height and misalignment (Section 2.7).

2.1. Air film pressure

The pressure $p_i(x, y)$ in each lubricating air film is calculated via the generalized Reynolds equation in [19]. Herein, the density ρ and the viscosity η are determined using an averaged fluid temperature $T_{m,i}(x, y)$. The latter is calculated by averaging the air film temperature T_i (see Section 2.4) over the gap height H_i (see Section 2.7), cf. [20]. Note that the index i refers to the number of the bearing pad:

$$\frac{\partial}{\partial x} \left[\frac{\rho(p_i, T_{m,i}) H_i^3}{12\eta(T_{m,i})} \frac{\partial p_i}{\partial x} \right] + \frac{\partial}{\partial y} \left[\frac{\rho(p_i, T_{m,i}) H_i^3}{12\eta(T_{m,i})} \frac{\partial p_i}{\partial y} \right] = \frac{\partial}{\partial x} \left[\frac{\rho(p_i, T_{m,i}) U H_i}{2} \right] + \frac{\partial}{\partial y} \left[\frac{\rho(p_i, T_{m,i}) V H_i}{2} \right]. \quad (1)$$

The values $U = \Omega y$ and $V = -\Omega x$ describe the x - and y -component of the rotor disk velocity. The remaining parameters are listed in Table 1.

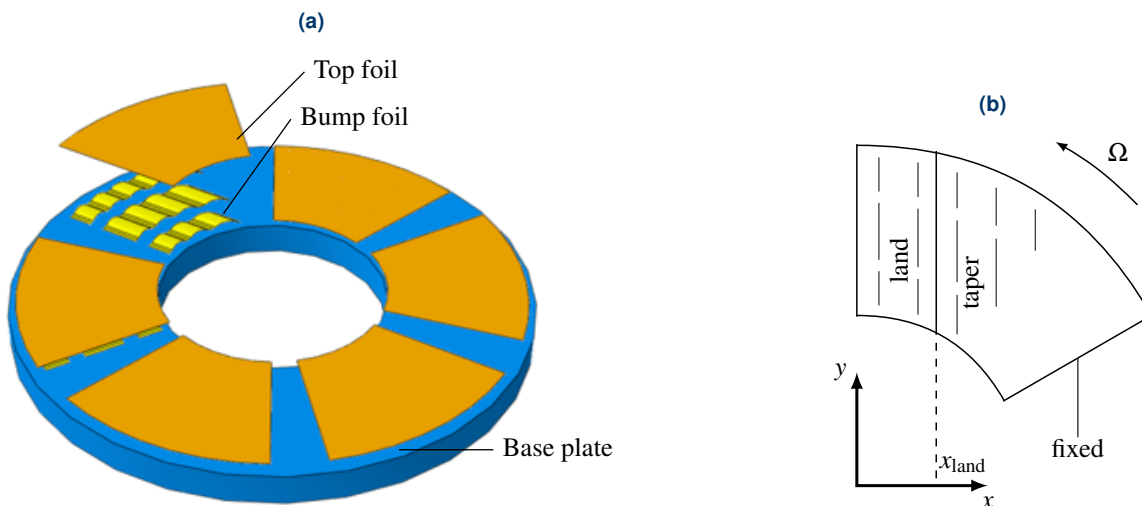


Fig. 1. Overview of the bearing design: (a) Foil thrust bearing with 6 pads consisting of a base plate as well as 6 individual bump and top foils and (b) taper-land profile of one individual bearing pad

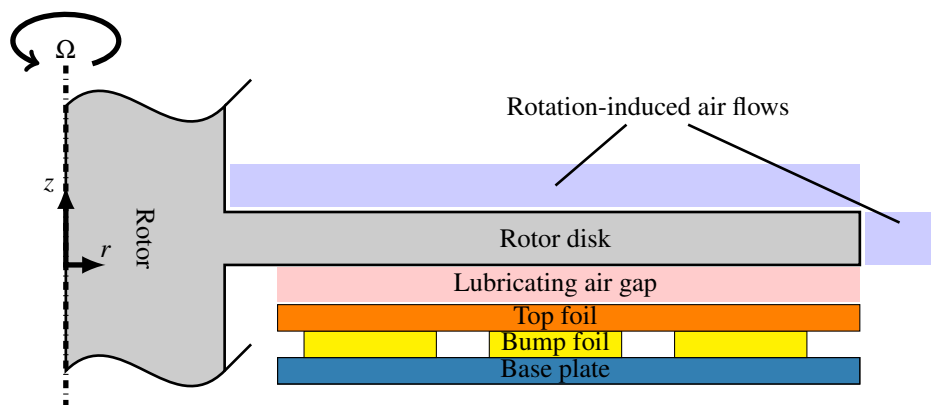


Fig. 2. Model components in cut view

Table 1
Air film parameters

Variable	Value	Description
ρ	$\frac{p}{RT_{m,i}}$	Density
R	0.287 kJ/(kg · K)	Gas constant of air
η	$\left[-1.75 \times 10^{-11} \left(\frac{T_{m,i}}{[K]}\right)^2 + 5.68 \times 10^{-8} \left(\frac{T_{m,i}}{[K]}\right) + 3.06 \times 10^{-6}\right] [\text{kg}/(\text{m} \cdot \text{s})]$	Viscosity

The 2D pad region on which equation (1) is solved is equivalent to the bearing pad depicted in Fig. 1b. Due to the sudden increase in film height at the outer borders of the bearing pad, the pressure at the pad edges is assumed to be at ambient pressure p_0 .

2.2. Top and bump foil deformations

This section describes the equations for the calculation of the deformations of top and bump foils in the thrust bearing. Table 2 lists the relevant parameters for the calculation of the foil deformations. For both types of foils, the Reissner-Mindlin shell theory [21] is applied. It allows for three translational degrees of freedom v_k with $k = \{1, 2, 3\}$ and two rotational degrees of freedom w_α with $\alpha = \{1, 2\}$ of the shell middle surface. The constitutive equations of the shell theory are:

$$\begin{aligned} q^\alpha &= Gt \cdot a^{\alpha\lambda} \gamma_\lambda \cdot k_S, \\ m^{\alpha\beta} &= BH^{\alpha\beta\lambda\mu} (\kappa_{\lambda\mu} - b_\lambda^\sigma \varphi_{\mu\sigma}), \\ n^{\alpha\beta} &= DH^{\alpha\beta\lambda\mu} \varphi_{\lambda\mu} - b_\rho^\beta m^{\alpha\rho}. \end{aligned} \quad (2)$$

Note that $n^{\alpha\beta}$ represents the stress resultant tensor, q^α is the transverse shear stress and $m^{\alpha\beta}$ is the moment tensor. The elasticity tensor $H^{\alpha\beta\lambda\mu}$ for a linear elastic, homogeneous and isotropic material reads as

$$H^{\alpha\beta\lambda\mu} = \frac{1-\nu}{2} \left(a^{\alpha\lambda} a^{\beta\mu} + a^{\alpha\mu} a^{\beta\lambda} + \frac{2\nu}{1-\nu} a^{\alpha\beta} a^{\lambda\mu} \right). \quad (3)$$

Table 2
Foil parameters

Variable	Value	Description
E	210 GPa	Young's modulus
ν	0.3	Poisson's ratio
t	75 μm 100 μm	Bump foil thickness Top foil thickness
k_S	5/6	Shear correction factor
$d_{i,T}$	30 mm	Top foil inner diameter
$d_{o,T}$	60 mm	Top foil outer diameter

In equation (2), $a^{\alpha\lambda}$ is the metric tensor, b_λ^σ is the curvature tensor, and k_S is the shear correction factor. Furthermore, D is the stretching stiffness, B is the bending stiffness, and Gt is the shear stiffness defined as

$$D = \frac{Et}{1-\nu^2}, \quad B = \frac{Et^3}{12(1-\nu^2)}, \quad Gt = \frac{Et}{2(1+\nu)}, \quad (4)$$

where E is Young's modulus and ν is Poisson's ratio of the steel foils. The three strain variables $\varphi_{\alpha\beta}$, $\kappa_{\alpha\beta}$, and γ_α are given as

$$\begin{aligned} \varphi_{\alpha\beta} &= v_{\beta|\alpha} - v_3 b_{\alpha\beta}, \\ \kappa_{\alpha\beta} &= \frac{1}{2} (w_{\alpha|\beta} + w_{\beta|\alpha}), \\ \gamma_\alpha &= w_\alpha + v_{3,\alpha} + v_\lambda b_\alpha^\lambda. \end{aligned} \quad (5)$$

Finally, the equilibrium equations read as follows:

$$\begin{aligned} -p^\beta &= n^{\alpha\beta} |_\alpha - q^\alpha b_\beta^\alpha, \\ -p^3 &= n^{\alpha\beta} b_{\alpha\beta} + q^\alpha |_\alpha, \\ 0 &= m^{\alpha\beta} |_\alpha - q^\beta. \end{aligned} \quad (6)$$

Herein, $\vec{p} = p^\alpha \vec{a}_\alpha + p^3 \vec{a}_3$ are the external forces and $\vec{n}^\alpha = n^{\alpha\beta} \vec{a}_\beta + q^\alpha \vec{a}_3$ and $\vec{m}^\alpha = m^{\alpha\beta} \vec{a}_3 \times \vec{a}_\beta$ are the internal force variables.

External forces on the top foils originate from the pressure in the lubricating air gap. Therefore, the air film pressure is implemented as an external load in the calculation of the top foil deflections. On the other hand, the resulting top foil deformations influence the gap function and – in turn – change the pressure profile in the lubricating air gap. For details on the height function see Section 2.7.

Contacts between the top foil and the bump foil as well as between the bump foil and the base plate are included in the model. The normal contact force F_N is implemented using a penalty formulation, $F_N = c \Delta v_3$, $c = 1 \times 10^{11}$ N/m being the penalty stiffness and Δv_3 the penetration depth.

The tangential behavior between top and bump foil is modeled via a stick-slip approach with regularized Coulomb friction, cf. [22]. The tangential force $F_T = \mu \cdot \text{step}(\Delta v_T) F_N$ acts in the direction opposite to the relative sliding motion Δv_T . μ is the friction coefficient ($\mu = 0.1$ assumed here for all contacts) and step describes a regularized sign function with a small transition zone. In this way, the foil sandwich is represented as a 2D nonlinear structural shell model. The nonlinearity arises from the contact formulation.

It should finally be mentioned that thermal deformations of the foils are not considered in this model. Although the thermal behavior of the thrust bearing is crucial for safe operation, thermal expansion of the top foil can be neglected as it causes in-plane deformations and does not contribute to changes in the lubricating gap height. Furthermore, the design of the bearing with individual pads and independent top and bump foils reduces the impact of thermal deformations further. The top foil temperature and the heat conduction through the bump foil is discussed in Section 2.6.

2.3. Rotor deformations

Due to the high angular velocity Ω , the rotor and rotor disk are modeled with an axisymmetric model, both for the rotor deformations $v_r(r, z)$ in radial and $v_z(r, z)$ in axial direction and the rotor temperature T_R (see Section 2.5). The deformations are obtained through the Navier-Lamé equations with centrifugal forces and thermal stresses, cf. [23, 24]:

$$\begin{aligned} \mu_R \left(\nabla^2 v_r - \frac{v_r}{r^2} \right) + (\gamma_R + \mu_R) \frac{\partial}{\partial r} \left(\frac{1}{r} \frac{\partial}{\partial r} (r v_r) + \frac{\partial v_z}{\partial z} \right) \\ - \varepsilon_R \frac{\partial \Delta T_R}{\partial r} = -\rho_R r \Omega^2, \\ \mu_R \nabla^2 v_z + (\gamma_R + \mu_R) \frac{\partial}{\partial z} \left(\frac{1}{r} \frac{\partial}{\partial r} (r v_r) + \frac{\partial v_z}{\partial z} \right) \\ - \varepsilon_R \frac{\partial \Delta T_R}{\partial r} = 0 \end{aligned} \quad (7)$$

with

$$\begin{aligned} \gamma_R &= \frac{E_R \nu_R}{(1 + \nu_R)(1 - 2\nu_R)}, \\ \mu_R &= \frac{E_R}{2(1 + \nu_R)}, \\ \varepsilon_R &= \frac{E_R \alpha_R}{1 - 2\nu_R}. \end{aligned} \quad (8)$$

γ_R is the Lamé constant and μ_R is the shear modulus. The constant ε_R describes thermoelastic stresses with $\Delta T_R = T_R - T_{\text{ref}}$ being the disk temperature difference with respect to a reference temperature $T_{\text{ref}} = T_0 = 20^\circ\text{C}$. Further, ρ_R is the density, α_R is the thermal expansion coefficient, E_R is Young's modulus, and ν_R is Poisson's ratio of the rotor material. Table 3 lists the relevant parameters for the calculation of the rotor deformations.

Table 3
Rotor parameters

Variable	Value	Description
E_R	210 GPa	Young's modulus
ν_R	0.3	Poisson's ratio
α_R	$13 \times 10^{-6} \text{K}^{-1}$	Thermal expansion coefficient

2.4. Air film temperature

The temperature field $T_{A,i}(x, y, z)$ of each sector is obtained from the 3D compressible energy equation, cf. for example [11]:

$$\begin{aligned} \rho c_P \left[u \frac{\partial T_{A,i}}{\partial x} + v \frac{\partial T_{A,i}}{\partial y} \right] = \left[\frac{\partial}{\partial z} \left(\lambda \frac{\partial T_{A,i}}{\partial z} \right) \right] \\ + \left[u \frac{\partial p}{\partial x} + v \frac{\partial p}{\partial y} \right] + \eta \left[\left(\frac{\partial u}{\partial z} \right)^2 + \left(\frac{\partial v}{\partial z} \right)^2 \right]. \end{aligned} \quad (9)$$

The four terms describe the convective heat transfer, diffusive heat transfer (conduction), the power of pressure forces, and

dissipation resulting from shear forces, respectively. λ is the heat conductivity, c_P is the heat capacity, and u and v are the x - and y -velocities of the lubricating air. Table 4 lists the definition of the heat capacity and the heat conductivity of air depending on the air temperature.

Table 4
Energy equation parameters

Variable	Value	Description
c_P	$\left[2.43 \times 10^{-4} \left(\frac{T_{A,i}}{[K]} \right)^2 - 7.7 \times 10^{-2} \left(\frac{T_{A,i}}{[K]} \right) + 1008 \right] [\text{J}/(\text{kg} \cdot \text{K})]$	Heat capacity
λ	$\left[-2.1 \times 10^{-8} \left(\frac{T_{A,i}}{[K]} \right)^2 + 8.46 \times 10^{-5} \left(\frac{T_{A,i}}{[K]} \right) + 2.89 \times 10^{-3} \right] [\text{W}/(\text{m} \cdot \text{K})]$	Heat conductivity

At the interfaces of the air films to the respective top foils, the temperature $T_{A,i}$ is coupled via interface conditions to the top foil temperature T_T (see Section 2.6), i.e. temperatures and heat fluxes are set to be equal. At the inlet boundary of the lubricating gap, the temperature is assumed to be the same as the rotor disk temperature. This assumption has been shown to be a good approximation, see [17, 25]. As the model contains 6 individual air films and a single rotor model, the heat fluxes of all air film sectors into the rotor disk can be given as a flux boundary condition for the rotor disk temperature. For the individual air films, the temperature at the interface to the rotor disk is set to the rotor disk temperature T_R (see Section 2.5).

2.5. Rotor temperature

The rotor and rotor disk temperature $T_R(r, z)$ is calculated via the heat conduction equation

$$\frac{\partial}{\partial r} \left[\lambda_R r \frac{\partial T_R}{\partial r} \right] + \frac{\partial}{\partial z} \left[\lambda_R r \frac{\partial T_R}{\partial z} \right] = 0. \quad (10)$$

The heat conduction of the rotor material is $\lambda_R = 12 \text{W}/(\text{m} \cdot \text{K})$. The boundary conditions of the rotor and rotor disk are crucial for the determination of the rotor temperature T_R . As mentioned in Section 2.4, the incoming heat flux into the rotor disk from all lubricating air gaps is enforced as a heat flux boundary condition at the interface to the bearing pad, cf. [17]. The heat flux $q_{\text{gap},i}(r)$ of each individual air film can be calculated as

$$q_{\text{gap},i}(r) = \frac{1}{2\pi} \int_{\varphi_l}^{\varphi_l} \left(\lambda \frac{\partial T_{A,i}}{\partial z} \right) \Big|_{\text{Interface}} r d\varphi, \quad (11)$$

where the temperature gradient is evaluated at the interface to the rotor disk. The angles φ_l and φ_t are the angles of the leading

edge and the trailing edge of the bearing pad, respectively. The total heat flux $q_{\text{gap}}(r)$ into the rotor disk now reads as follows:

$$q_{\text{gap}}(r) = \sum_{i=1}^6 q_{\text{gap},i}(r). \quad (12)$$

At the backside of the rotor disk, the disk rotation causes an airflow. The heat flux that leaves the disk is calculated from the temperature $T_C(r, z)$ in this region which is obtained from the energy equation (assuming axisymmetry):

$$\frac{\partial}{\partial z} \left[\lambda_{C,\text{eff}} \frac{\partial T_C}{\partial z} \right] = \rho_C c_{P,C} \left[u_C \frac{\partial T_C}{\partial r} + w_C \frac{\partial T_C}{\partial z} \right] - \rho_C (v_C + v_{CT}) \left[\left(\frac{\partial u_C}{\partial z} \right)^2 + \left(\frac{\partial v_C}{\partial z} \right)^2 \right]. \quad (13)$$

Here, $\lambda_{C,\text{eff}}$ is an effective thermal conductivity according to [26], ρ_C the density, $c_{P,C}$ the isochoric heat capacity and v_C and v_{CT} are the kinematic viscosity and the turbulent kinematic viscosity according to Cebeci and Smith [27]. The velocity field consisting of the radial velocity u_C , the circumferential velocity v_C and the velocity w_C in z -direction is calculated from the boundary layer equations for steady incompressible axisymmetric flow (neglecting a radial pressure gradient), see [27].

In the radial gap between the rotor disk and the housing, the disk rotation also causes an airflow. It is assumed to be laminar with purely circumferential flow (Couette flow) and with linearly decreasing velocity over the radial coordinate (disk speed at the inner boundary, zero speed at the outer boundary). This simple assumption is made as the initial gap width t is 200 μm and decreases below 100 μm at high rotational speeds due to centrifugal effects. Thus, the 2D energy equation

$$\frac{\partial}{\partial r} \left[\lambda_{RG} r \frac{\partial T_{RG}}{\partial r} \right] + \frac{\partial}{\partial z} \left[\lambda_{RG} r \frac{\partial T_{RG}}{\partial z} \right] = -r \eta_{RG} \left[\frac{\Omega r_D}{t} \right]^2 \quad (14)$$

including dissipative heating is solved to obtain the temperature profile $T_{RG}(r, z)$ in the radial gap. In equation (14), λ_{RG} is the thermal conductivity, η_{RG} is the dynamic viscosity of air in the radial gap, r_D is the disk radius and t is the gap width with account of disk deformations.

2.6. Top foil temperature

The top foil temperature profile $T_{T,i}(x, y)$ of each top foil is obtained by the planar heat conduction equation

$$-\lambda_T t_T \Delta T_{T,i} = q_{T,\text{in}} + q_{T,\text{out}} \quad (15)$$

with constant heat conductivity $\lambda_T = 12 \text{ W}/(\text{m} \cdot \text{K})$ and thickness t_T of the top foils. The heat fluxes $q_{T,\text{in}} = \left(\lambda \frac{\partial T_{A,i}}{\partial z} \right) \Big|_{\text{Interface}}$ as well as $q_{T,\text{out}} = q_b$ at the contact lines and $q_{T,\text{out}} = q_c$ everywhere else is solved. Over each top foil, an incoming heat flux from the lubricating gap is calculated. A possible cooling heat flux q_c originating from active cooling can be implemented as well, but is neglected in the present study. Heat conduction from each top foil into the base plate

is modeled as an outgoing heat flux $q_b = -\frac{2}{R_{\text{th}}}(T_{T,i} - T_{\text{Base}})$ at the contact lines between top and bump foil, visible in Fig. 1b. Herein, $R_{\text{th}} = R_{\text{TB,air}} + R_{\text{bump}} + R_{\text{BB,air}}$ is the thermal resistance of a half bump arc composed of the thermal contact resistance between top and bump foil $R_{\text{TB,air}}$, thermal conduction resistance of the half-bump arc R_{bump} and the contact resistance between bump foil and base plate $R_{\text{BB,air}}$, cf. [28]. The leading edge of the top foil is assumed to have the same temperature as the air at the inlet. On the remaining three boundaries, a zero heat flux condition is imposed. Note that the influence of the pressure acting upon the foil sandwich is of subordinate importance for the thermal contact resistances [17].

2.7. Air film height and misalignment

For the numerical analysis of the thrust bearing, the film height function $H(x, y)$ is crucial. It is affected by the bearing design, but also includes the deformations of the bearing components. Each bearing pad possesses an individual height function $H_i(x, y)$:

$$H_i(x, y) = z_R - v_{3,T,i} + v_z(z=0, r) + H_{\text{mis}}. \quad (16)$$

Herein, $v_{3,T,i}$ is the deformation of the i -th top foil and is individual for each pad. The remaining values are the same for each bearing pad: z_R displays the axial position of the rotor, $v_z(z=0, r)$ is the deformation of the rotor disk underside (see Fig. 2), and H_{mis} represents the misalignment between the rotor disk and the bearing:

$$H_{\text{mis}} = -\tan(\beta_{\text{mis}})x + \frac{\tan(\alpha_{\text{mis}})}{\cos(\beta_{\text{mis}})}y. \quad (17)$$

The two misalignment angles α_{mis} and β_{mis} are displayed in Fig. 3.

2.8. Computational details

This section describes details of the computation of the fully coupled TEHD FE model. The model has roughly 2.1 million degrees of freedom (DOF) plus approximately 320 000 internal DOFs. A direct MUMPS solver is used to find the stationary solution for a given set of parameters. While the bearing design and the underlying geometrical parameters for the various components obviously play a key role in the performance of thrust bearings, the main parameters for the presented study comprise the angular velocity Ω , the minimal gap height H_{min} and the misalignment angles α_{mis} and β_{mis} .

In order to generate a solution for the full model, a multi-step approach is used for convergence improvement. This approach starts with different segregated parts of the model (energy equation, shell equations, surrounding) in order to generate adequate starting solutions for the complete fully coupled model. The first fully coupled simulation starts with very low rotational speeds and relatively large gap heights (i.e. low loads) and without misalignment of the components. In the next step, the rotational speed is increased in steps up to the desired speed of 100krpm. Next, the minimal gap height parameter H_{min} is decreased in order to obtain higher loads. In the last step, the

M. Eickhoff, J. Triebwasser, and B. Schweizer

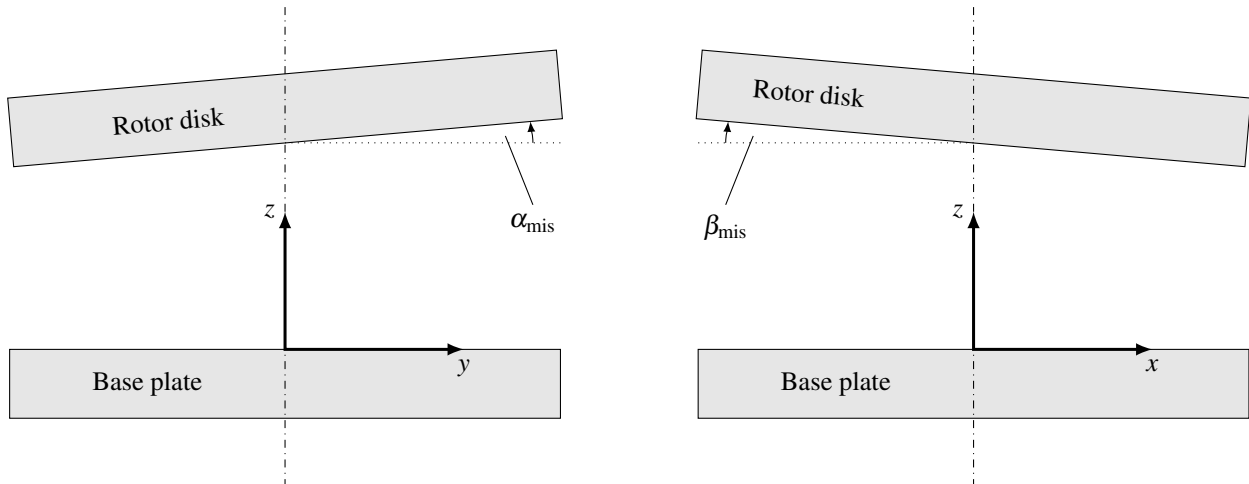


Fig. 3. Definition of the two misalignment angles α_{mis} and β_{mis} of equation (17)

misalignment angles may be increased to study the influence of misalignment.

On a local machine (Win 7) with a 4th generation Intel Xeon processor with 12 logical cores and 128 GB of RAM, the described process of generating a full solution with the model takes approximately 40 hours. It should be mentioned that computation times increase significantly with increasing misalignment angles. Compared to the corresponding single-pad model, computation times are increased by a factor of 8–10.

3. RESULTS

This section presents numerical results of the fully coupled TEHD model considering misalignment. In Fig. 4, the nominal design height function and the real height function are compared. While the nominal height function without deformations in Fig. 4a shows the ideal taper-land topology, Fig. 4b shows the deformed height function which is affected by the top foil deformations as well as the rotor disk deformations. As the top foil is subject to pressure loading from the lubricating air gap,

it is forced downwards onto the bump foil support. As the contact between top and bump foils only forms at the peak line of the bumps, the top foil does not possess any structural support in between these lines, cf. Fig. 4b. The sagging of the top foil between the bump lines is widely known as top foil sagging effect. It is responsible for a degradation of the height function and a decrease in load capacity.

Deformations of the rotor disk stem from centrifugal forces as well as axial temperature gradients. Figure 5 displays the rotor disk temperature for a rotational speed of 100krpm and a power loss of 154 W. The underside of the rotor disk is at the interface to the lubricating air gaps where dissipation causes high air temperatures. The dissipation is dependent on the shear velocity within the air film. Therefore, the rotor disk temperature is highest near its outer radius where circumferential velocities are highest. Towards the base of the rotor disk (attachment to the rotor) and towards the backside of the disk, its temperature gets cooler. The temperature gradient of the rotor disk temperature, which is proportional to the heat flux, is also depicted in Fig. 5 by black arrows.

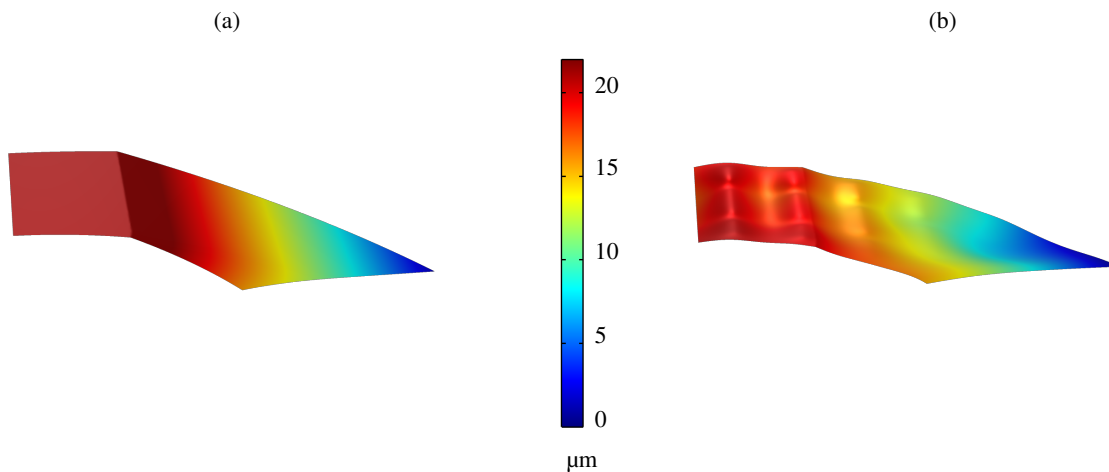


Fig. 4. Height function (relative scale) of equation (16) without misalignment: (a) nominal height function without deformations $v_{3,T}$ and $v_z(z=0, r)$ and (b) height function with top foil and rotor disk deformations showing top foil sagging

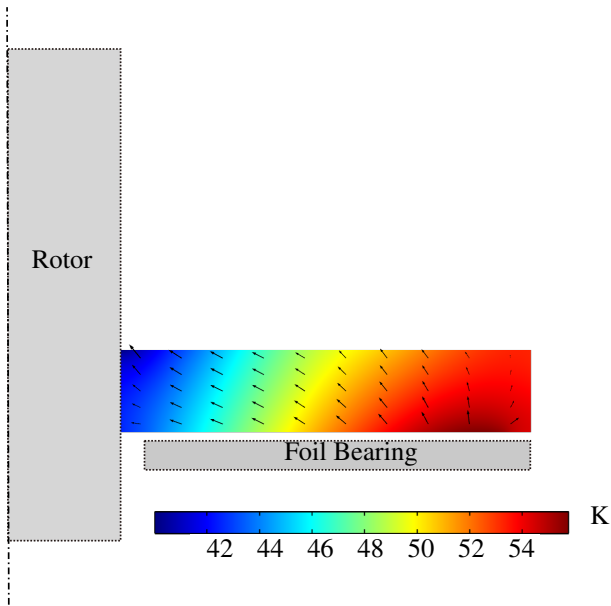


Fig. 5. Rotor disk temperature $T_R - T_0$ as well as rotor disk temperature gradient marked by black arrows

The axial temperature gradient of the rotor disk causes thermal bending and is included in the deformed height function of Fig. 4b.

Figure 6 now displays the pressure distributions p_i for all bearing pads with different misalignment angles α_{mis} . Note that the second misalignment angle β_{mis} is set to 0 in all studies. The pressure profiles are displayed on a common pressure scale also depicted in Fig. 6. As expected, the case without misalignment between the rotor disk and the bearing ($\alpha_{\text{mis}} = \beta_{\text{mis}} = 0 \text{ rad}$) yields identical pressure distributions across all bearing pads. In general, the highest pressures are observed in the land region of the pad with distinct pressure peaks at the contact lines between top foils and bump foils. These contact lines are marked by black lines in Fig. 6. Please note again that the direction of rotation of the rotor disk in the displayed views is counter-clockwise (positive z -direction).

When the misalignment angle is increased in Figs. 6b-d, the rotor disk tilts towards the lower half of the bearing (negative y -direction). For comparability, all simulations were carried out with a constant minimal air gap height. While all six pads of Fig. 6a (no misalignment) show a spot where this minimal gap

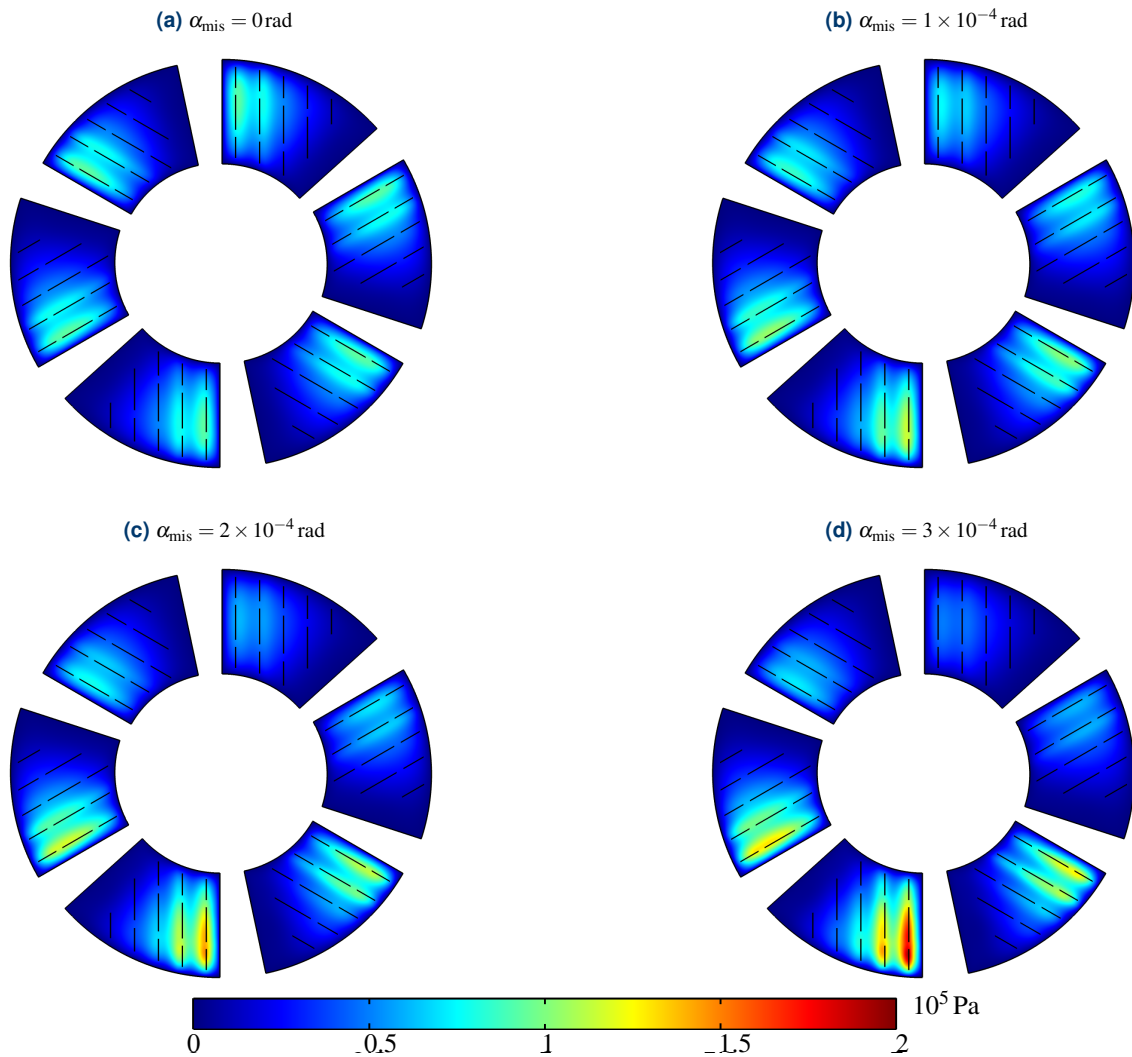


Fig. 6. Pressure distributions $p_i - p_0$ for various misalignment angles α_{mis}

height is observed, for the remaining cases, the minimal gap height is only achieved on the bottom left pad in Figs. 6b–d. It is interesting to notice that – by contrast to rigid thrust bearings – the compliant foil thrust bearing can compensate a portion of the misalignment. This is why the bearing pads in the top half of Figs. 6b–d still show significant pressure buildup. For the last case of Fig. 6d, the pad with the highest load generates two times as much load capacity as the least loaded pad on the top right. However, the overall load capacity of the bearing is very similar with a value of 55 N at a rotational speed of 100 krpm at a minimal gap height of $5 \mu\text{m}$ when compared to results without misalignment. The compliant foil thrust bearing is able to compensate and still show similar load capacities. Figure 7 shows the thrust load over the misalignment angle α_{mis} . For the investigated misalignment angle range, the thrust load is nearly constant. As a downside, the power loss of the thrust bearing is increased due to the uneven loading.

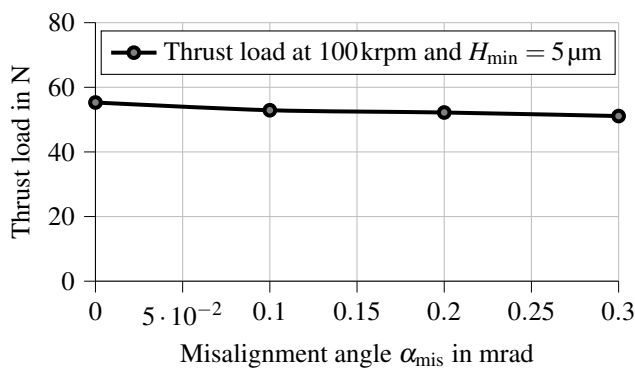


Fig. 7. Thrust load over the misalignment angle α_{mis}

Simultaneously, through the uneven loading of the bearing, the exerted power loss increases by approximately 6.5% to 164 W.

Short remark on the misalignment angles displayed in this manuscript: A misalignment configuration with $\alpha_{\text{mis}} = 1 \times 10^{-4}$ rad and $\beta_{\text{mis}} = 0$ rad refers to a maximum misalignment of $3 \mu\text{m}$ at the outer radius of the thrust bearing.

Figure 8 shows the impact of thermal bending of the rotor disk. The 3D image of the disk as well as the cross-sectional view both show a dished rotor disk. The graph at the bottom of the figure displays the axial deformation of the disk on the side facing the thrust bearing. It is typical for this hot side of the rotor disk to bend away from the bearing due to an axial temperature gradient inside the rotor disk. At the outer radius of the disk, the resulting bending is substantial and causes an uneven gap height, which in turn reduces the load capacity of the bearing.

Figure 9 shows the air film temperature in all six bearing sectors via a slice plot for the misalignment case of $\alpha_{\text{mis}} = 3 \times 10^{-4}$ rad. Herein, the top slice corresponds to the interface with the rotor disk. Note again that the rotor disk temperature does not depend on the circumferential coordinate. Therefore, the top slice temperature is equal for all bearing sectors. Differences are observed when the bottom slice of the air film temper-

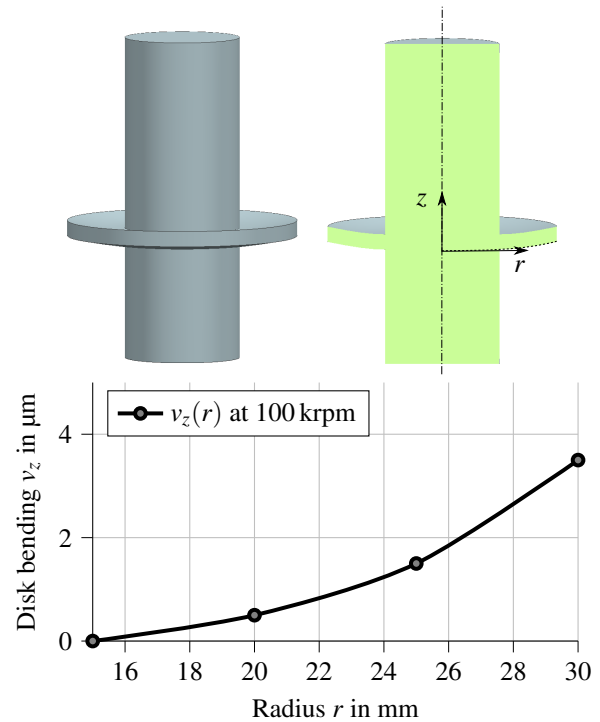


Fig. 8. Rotor disk bending (dishing) illustrated in a 3D view of the rotor shaft and the rotor disk as well as a cross section view, graph (bottom) shows the axial rotor disk deformation v_z over the radial coordinate r

atures is investigated. This slice corresponds to the interfaces with the top foils. In the bottom half of the bearing in Fig. 9, the maximum temperatures are slightly higher than those in the top half due to higher power losses in the lubricating air film.

The temperature distribution in the air films is qualitatively similar with two distinct patterns: a temperature rise towards the outer edge due to higher dissipation as well as temperature drops near the contact lines of top and bump foil due to the heat conduction through the bumps into the base plate.

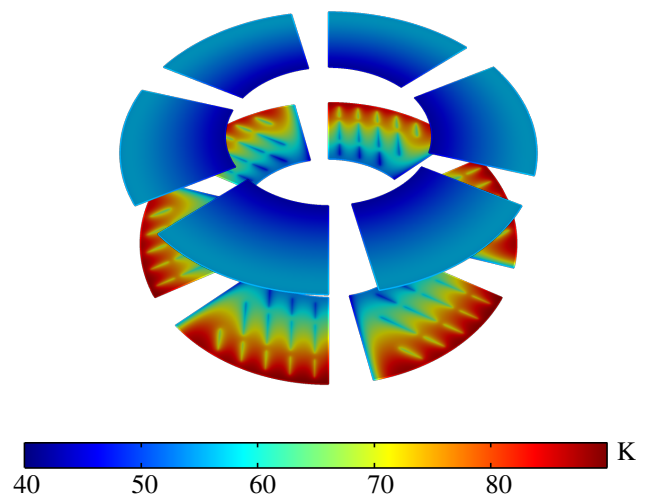


Fig. 9. Air film temperatures $T_{A,i} - T_0$ in slices at the top foil interface and at the rotor disk interface for $\alpha_{\text{mis}} = 3 \times 10^{-4}$ rad

4. CONCLUSIONS

A detailed TEHD model for air-foil thrust bearings considering misalignment between the rotor disk and the bearing has been presented. The model contains an in-depth description of the foil deformations via a shell model as well as a model for rotor and rotor disk deflections. The 2D compressible Reynolds equation and the 3D energy equation are solved for each bearing pad. Furthermore, the temperatures of the top foils, the rotor, and the surrounding air are calculated in the model. This allows for the fully coupled analysis of bump-type thrust bearings with full account of the thermal influences of individual pads when misalignment is present.

Numerical results with this model show the influence of component deformations on the height function and, subsequently, on the bearing performance. The initial taper-land height function is degraded by top foil sagging and thermal bending of the rotor disk. While top foil sagging is caused by the pressure load onto the top foil combined with line-type support of the bump foil understructure, thermal bending of the rotor disk is a result of the axial temperature gradient in the rotor disk. This temperature gradient is caused by the hot temperatures in the lubricating gap through dissipation on the one hand and the cooling of the rotor disk through conduction into the surroundings on the other hand. The rotation-induced airflows around the runner disk at the outer perimeter and at the disk backside play a key role in this regard.

It is shown that misalignment causes an uneven distribution of the load onto the bearing pads. However, results indicate that, for the presented misalignment cases, the compliant foil thrust bearing was able to compensate and still show similar load capacities. As a downside, the power loss of the thrust bearing is increased due to the uneven loading.

Through the modeling of the full bearing with account for all individual bearing pads with individual height functions, small temperature differences in the lubricating air temperature can be observed. The computational effort for each simulation is highly increased when compared to a model with a reduced approach considering only a single bearing pad. By contrast to the reduced investigation, only this fully coupled approach is appropriate for TEHD simulations with misalignment. The detailed model allows for the investigation of foil thrust bearings under misalignment conditions in great depth. However, with this level of model complexity, an extensive parameter variation for geometrical dimensions is no longer possible.

REFERENCES

- [1] G.L. Agrawal, "Foil air/gas bearing technology – an overview," in *Volume 1: Aircraft Engine; Marine; Turbomachinery; Micro-turbines and Small Turbomachinery*, ser. Turbo Expo: Power for Land, Sea, and Air. American Society of Mechanical Engineers, 1997, p. V001T04A006, doi: [10.1115/97-GT-347](https://doi.org/10.1115/97-GT-347).
- [2] P. Samanta, N. Murmu, and M. Khonsari, "The evolution of foil bearing technology," *Tribol. Int.*, vol. 135, pp. 305–323, 2019.
- [3] K.C. Radil and C. DellaCorte, "The effect of journal roughness and foil coatings on the performance of heavily loaded foil air bearings," *Tribol. Trans.*, vol. 45, no. 2, pp. 199–204, 2002.
- [4] F. Balducchi, M. Arghir, R. Gauthier, and E. Renard, "Experimental Analysis of the Start-Up Torque of a Mildly Loaded Foil Thrust Bearing1," *J. Tribol.*, vol. 135, no. 3, 2013, doi: [10.1115/1.4024211](https://doi.org/10.1115/1.4024211).
- [5] B.D. Dykas, "Factors influencing the performance of foil gas thrust bearings for oil-free turbomachinery applications," Ph.D. dissertation, Case Western Reserve University, 2006.
- [6] F. Balducchi, M. Arghir, and R. Gauthier, "Experimental analysis of the dynamic characteristics of a foil thrust bearing," *J. Tribol.*, vol. 137, no. 2, p. 021703, 2015.
- [7] N. LaTray and D. Kim, "Design of Novel Gas Foil Thrust Bearings and Test Validation in a High-Speed Test Rig," *J. Tribol.*, vol. 142, no. 7, p. 071803, 2020, doi: [10.1115/1.4046412](https://doi.org/10.1115/1.4046412).
- [8] I. Iordanoff, "Analysis of an aerodynamic compliant foil thrust bearing: Method for a rapid design," *J. Tribol.*, vol. 121, no. 4, pp. 816–822, 1999.
- [9] C.A. Heshmat, D.S. Xu, and H. Heshmat, "Analysis of gas lubricated foil thrust bearings using coupled finite element and finite difference methods," *J. Tribol.*, vol. 122, no. 1, pp. 199–204, 2000.
- [10] R.J. Bruckner, *Simulation and modeling of the hydrodynamic, thermal, and structural behavior of foil thrust bearings*. Case Western Reserve University, 2004.
- [11] D. Lee and D. Kim, "Thermohydrodynamic Analyses of Bump Air Foil Bearings With Detailed Thermal Model of Foil Structures and Rotor," *J. Tribol.*, vol. 132, no. 2, p. 021704, 2010, doi: [10.1115/1.4001014](https://doi.org/10.1115/1.4001014).
- [12] L. San Andrés and T. H. Kim, "Thermohydrodynamic Analysis of Bump Type Gas Foil Bearings: A Model Anchored to Test Data," *J. Eng. Gas Turbines Power*, vol. 132, no. 4, p. 042504, 2010, doi: [10.1115/1.3159386](https://doi.org/10.1115/1.3159386).
- [13] K. Sim and T. H. Kim, "Thermohydrodynamic analysis of bump-type gas foil bearings using bump thermal contact and inlet flow mixing models," *Tribol. Int.*, vol. 48, pp. 137–148, 2012, doi: [10.1016/j.triboint.2011.11.017](https://doi.org/10.1016/j.triboint.2011.11.017).
- [14] T. Conboy, "Real-gas effects in foil thrust bearings operating in the turbulent regime," *J. Tribol.*, vol. 135, no. 3, p. 031703, 2013.
- [15] K. Feng, L.-J. Liu, Z.-Y. Guo, and X.-Y. Zhao, "Parametric study on static and dynamic characteristics of bump-type gas foil thrust bearing for oil-free turbomachinery," *Proc. Inst. Mech. Eng. Part J.-J. Eng. Tribol.*, vol. 230, no. 8, pp. 944–961, 2016.
- [16] J.R. Dickman, "An investigation of gas foil thrust bearing performance and its influencing factors," Ph.D. dissertation, Case Western Reserve University, 2010.
- [17] A. Lehn, "Air Foil Thrust Bearings: A Thermo-Elasto-Hydrodynamic Analysis," Ph.D. thesis, Technische Universität Darmstadt, 2017.
- [18] M. Rieken, M. Mahner, and B. Schweizer, "Thermal Optimization of Air Foil Thrust Bearings Using Different Foil Materials," *J. Turbomach.*, vol. 142, no. 10, p. 101003, 2020, doi: [10.1115/1.4047633](https://doi.org/10.1115/1.4047633).
- [19] D. Dowson, "A generalized Reynolds equation for fluid-film lubrication," *Int. J. Mech. Sci.*, vol. 4, no. 2, pp. 159–170, 1962, doi: [10.1016/S0020-7403\(62\)80038-1](https://doi.org/10.1016/S0020-7403(62)80038-1).
- [20] D. Lee and D. Kim, "Three-Dimensional Thermohydrodynamic Analyses of Rayleigh Step Air Foil Thrust Bearing with Radially Arranged Bump Foils," *Tribol. Trans.*, vol. 54, no. 3, pp. 432–448, 2011, doi: [10.1080/10402004.2011.556314](https://doi.org/10.1080/10402004.2011.556314).
- [21] Y. Başar and W.B. Krätzig, *Mechanik der Flächentragwerke: Theorie, Berechnungsmethoden, Anwendungsbeispiele*, 1st ed., ser. Grundlagen der Ingenieurwissenschaften. Wiesbaden: Vieweg + Teubner Verlag, 1985, doi: [10.1007/978-3-322-93983-8](https://doi.org/10.1007/978-3-322-93983-8).

M. Eickhoff, J. Triebwasser, and B. Schweizer

- [22] P. Wriggers, *Computational contact mechanics*, 2nd ed. Berlin: Springer, 2006, doi: [10.1007/978-3-540-32609-0](https://doi.org/10.1007/978-3-540-32609-0).
- [23] M.H. Sadd, *Elasticity: Theory, Applications, and Numerics*. Elsevier, 2005.
- [24] M. Mahner, A. Lehn, and B. Schweizer, "Thermogas- and thermohydrodynamic simulation of thrust and slider bearings: Convergence and efficiency of different reduction approaches," *Tribol. Int.*, vol. 93, pp. 539–554, 2016, doi: [10.1016/j.triboint.2015.02.030](https://doi.org/10.1016/j.triboint.2015.02.030).
- [25] A. Lehn, M. Mahner, and B. Schweizer, "Characterization of static air foil thrust bearing performance: an elasto-gasdynamic analysis for aligned, distorted and misaligned operating conditions," *Arch. Appl. Mech.*, vol. 88, no. 5, pp. 705–728, 2018, doi: [10.1007/s00419-017-1337-7](https://doi.org/10.1007/s00419-017-1337-7).
- [26] C.L. Ong and J.M. Owen, "Computation of the flow and heat transfer due to a rotating disc," *Int. J. Heat Fluid Flow*, vol. 12, no. 2, pp. 106–115, 1991, doi: [10.1016/0142-727X\(91\)90036-U](https://doi.org/10.1016/0142-727X(91)90036-U).
- [27] T. Cebeci and A. Smith, *Analysis of Turbulent Boundary Layers*. New York: Academic Press, 1974.
- [28] A. Lehn, M. Mahner, and B. Schweizer, "A Contribution to the Thermal Modeling of Bump Type Air Foil Bearings: Analysis of the Thermal Resistance of Bump Foils," *J. Tribol.*, vol. 139, no. 6, p. 061702, 2017, doi: [10.1115/1.4036631](https://doi.org/10.1115/1.4036631).